

# Comprehensive high speed automotive SM-PMSM torque control stability analysis including novel control approach

A. Arias<sup>a,\*</sup>, E. Ibarra<sup>b</sup>, E. Tranco<sup>c</sup>, R. Griñó<sup>a</sup>, I. Kortabarria<sup>b</sup>, J. Caum<sup>d</sup>

<sup>a</sup> Institute of Industrial and Control Engineering, Universitat Politècnica de Catalunya, Diagonal, 647, 08028 Barcelona, Spain

<sup>b</sup> Department of Electronic Technology, UPV/EHU, C. Rafael Moreno, Ptxitxi, 48080 Bilbao, Spain

<sup>c</sup> Tecnalia Research and Innovation, Industry and Transport Unit, Parque Científico y Tecnológico de Bizkaia, c/ Geldo, Edif. 700, 48160 Derio, Spain

<sup>d</sup> Centre for Sensors Instruments and Systems Development, Universitat Politècnica de Catalunya, Rbla. Sant Nebridi, 08222 Terrassa, Spain

## ARTICLE INFO

### Keywords:

Discrete-time vector current control  
Decoupling  
Electric Vehicle (EV)  
Permanent Magnet Synchronous Machines (PMSM)  
High-speed AC electrical drives

## ABSTRACT

Permanent magnet synchronous machines (PMSM) are widely used in the automotive industry for electric vehicle (EV) and hybrid electric vehicle (HEV) propulsion systems, where the trend is to achieve high mechanical speeds. High speeds inevitably imply high current electrical frequencies, which can lead to a lack of controllability when using field oriented control (FOC) due to sampling period constraints. In this work, a comprehensive discrete-time model is fully developed to assess the stability issues in the widely used FOC. A speed-adaptive control structure that overcomes these stability problems and extends the speed operation range of the PMSM is presented. Also, a numerical methodology from which the maximum operating stable frequency can be computed in advance of any experimentation, is developed. All contributions are accompanied and supported by numerical results obtained from an accurate MATLAB/Simulink model.

## 1. Introduction

In recent years, global warming and climate change have lead to the development of new electric vehicle (EV) and hybrid electric vehicle (HEV) technologies. According to the latest International Energy Agency Global EV Outlook report (2018), the combination of the high efficiency of electric motors and low-carbon electricity production will allow EVs to significantly reduce CO<sub>2</sub> emissions with respect to internal combustion engine based vehicles. On a well-to-wheel basis, EVs in Europe will reduce CO<sub>2</sub> emissions in about 50% with respect to gasoline cars, and in 40% with respect to diesel cars [1]. For all these reasons, it is expected that market penetration of HEV/EVs will increase exponentially in the next few years [2,3].

The propulsion system can be considered as the core element in modern HEV/EVs. In general, such systems are constituted by a power converter, an electric machine and their corresponding control electronics. In this context, a great variety of electric machine technologies can be found in HEV/EVs, such as induction machines (IM), permanent magnet synchronous machines (PMSM), synchronous reluctance machines (SynRM) and switched reluctance machines (SRM) [4–6]. Among them, PMSMs are the preferred option due to their high power density, high efficiency and simple structure [7–11]. Depending on the

configuration of the rotor magnets, two PMSM machine technologies, i.e., interior (IPMSM) and surface mounted (SM-PMSM) machines can be differentiated. Thanks to the additional reluctant torque, IPMSMs have the highest power density. Thus, this technology is extensively used on HEVs (Toyota Prius, for example), in which drive volume is a critical factor [12]. In contrast, SM-PMSMs have a simpler construction, lower rotor inertia, and the adjustment of the control scheme is easier. For these reasons, SM-PMSMs can be found in a number of EV applications (where space constraints are not as tight as in HEVs) [13,14]. For example, industrial manufacturers such as GKN/EVO (AF series) and Yasa (400 series) produce automotive grade axial flux SM-PMSMs. In particular, this paper will focus on this type of machine.

Currently, HEV/EVs mount PMSMs whose mechanical speeds can be up to 15000 r/min [4,5], although, in general, maximum speed is around 4000–8000 r/min. Taking into account the multi-pole design of such PMSMs, electric frequencies in the range of 300–600 Hz are common in the fundamental components of stator voltages and currents synthesized by the power converter. The European Union Horizon 2020 program call “Next generation electric drivetrains for fully electric vehicles, focusing on high efficiency and low cost” and a number of papers [15,16] forecast that the next generation of electric motors will become faster, allowing to reduce the machine size for the same rated mechanical

\* Corresponding author.

E-mail addresses: [antoni.arias@upc.edu](mailto:antoni.arias@upc.edu) (A. Arias), [edorta.ibarra@ehu.eus](mailto:edorta.ibarra@ehu.eus) (E. Ibarra), [elena.tranco@tecnalia.com](mailto:elena.tranco@tecnalia.com) (E. Tranco), [roberto.grino@upc.edu](mailto:roberto.grino@upc.edu) (R. Griñó), [inigo.kortabarria@ehu.eus](mailto:inigo.kortabarria@ehu.eus) (I. Kortabarria), [jesus.caum@upc.edu](mailto:jesus.caum@upc.edu) (J. Caum).

<https://doi.org/10.1016/j.ijepes.2019.02.035>

Received 19 September 2018; Received in revised form 10 December 2018; Accepted 18 February 2019

0142-0615/ © 2019 Elsevier Ltd. All rights reserved.

**List of acronyms**

DSP	Digital signal processor
DTC	Direct torque control
ECU	Electronic control unit
EMF	Electromotive force
EV	Electric vehicle
FOC	Field oriented control
HSEM	High speed electric machine
HEV	Hybrid electric vehicle
IGBT	Insulated gate bipolar transistor
IM	Induction machine
LTI	Linear time invariant
LPV	Linear parameter variant
LTV	Linear time variant

MIMO	Multi input multi output
MBD	Model based design
PI	Proportional integral
PMSM	Permanent magnet synchronous machine
PF	Pre-filter
PWM	Pulse width modulation
SISO	Single input single output
SM-PMSM	Surface mounted permanent magnet synchronous machine
STATCOM	Static compensator
SRM	Switched reluctance machine
SynRM	Synchronous reluctance machine
VOC	Voltage oriented controller
VSI	Voltage source inverter
ZOH	Zero-order hold

power. In this context, two control aspects must be considered for high speed control of PMSM machines:

- Due to DC-link voltage constraints, field weakening control is required at high speeds. This aspect has been thoroughly studied in the scientific literature, providing robust solutions even under parameter uncertainties [12,17–19].
- Machine stability issues can occur at high speeds. This can be challenging from the electric machine torque control algorithm point of view, especially if current insulated gate bipolar transistor (IGBT) technologies operating with switching frequencies up to 10 kHz are used to constitute the power inverter. Thus, it is important to understand the limitations of conventional control structures due to their corresponding sample time constraints.

A variety of PMSM control approaches such as direct torque control (DTC) [20–22], predictive control [23] and adaptive structures [24,25], can be found in the scientific literature and in the industry. However, field oriented control (FOC) is by far the most common torque control strategy employed for PMSM drives [12,26–29]. In this paper, the influence of the speed in the conventional FOC control structure is studied theoretically and by simulation. In order of extending the speed operation range of the machine, a novel adaptive control algorithm is proposed and its stability analysis, from which the maximum frequency can be computed, is reported. Simulation results that validate the proposed approach are presented.

It is important to point out that although this article focuses on machine stability at high speed operation, such stability issue might potentially appear also in grid connected converters applications with dq current controllers [30], such as static compensators (STATCOM) [31] and voltage oriented controllers (VOC) [32]. Thus, the mathematical tools provided in this paper can be reused for a variety of applications.

## 2. Automotive SM-PMSM fundamentals

In general, flux linkage of current automotive axial flux SM-PMSMs has a linear behaviour, as magnetic saturation is negligible for such particular machine designs. For this reason, the stator inductances and PM flux linkage can be considered constant, with independence of the operation point (torque/speed) of the machine. Thus, the equations that represent the stator voltages of SM-PMSMs in the dq synchronous rotating reference frame are:

$$v_d = Ri_d + L_d \frac{di_d}{dt} - \omega L_q i_q, \quad (1)$$

$$v_q = Ri_q + L_q \frac{di_q}{dt} + \omega (L_d i_d + \Psi_m), \quad (2)$$

where  $v_d$ ,  $v_q$ ,  $i_d$  and  $i_q$  are the stator voltages and currents;  $R$ ,  $L_d$  and  $L_q$  are the stator resistance and inductances,  $\Psi_m$  is the magnetic flux of the permanent magnets and  $\omega$  is the electrical rotor angular speed ( $\omega = P\omega_m$ , where  $P$  is the PMSM pole-pair number). The electromagnetic torque produced by the PMSM is obtained as:

$$T_{em} = \frac{3}{2} P \{ \Psi_m i_q + (L_d - L_q) i_d i_q \}. \quad (3)$$

In SM-PMSMs, d- and q-axis stator inductances are equal ( $L_d = L_q$ ). As a consequence, the reluctant torque component is zero and only magnetic torque can be produced.

PMSM drives have voltage and torque production constraints, mainly due to inverter ratings and available DC-link voltage limitations [33]. These constraints, which arise at high speeds [17,34,35], can be represented with the following mathematical expressions:

$$\sqrt{i_d^2 + i_q^2} \leq I_{max}, \quad (4)$$

$$L_d^2 \left( i_d + \frac{\Psi_m}{L_d} \right)^2 + L_q^2 i_q^2 \leq \left( \frac{V_{max}}{\omega} \right)^2, \quad (5)$$

where  $I_{max}$  and  $V_{max}$  are the maximum allowable stator current and voltage, respectively [17,34,35].

## 3. FOC control at high speed operation

### 3.1. Traditional FOC control

When FOC control structure is used, machine stator currents are transformed into the synchronous dq reference frame as illustrated in Fig. 1. In order to achieve the EV target torque, an optimal current set point generator [17] sets the dq current references for a given EV operation point, considering both machine efficiency and field weakening operation. The reference voltages  $v_{uvw}^*$  are synthesized by modulating a voltage source inverter (VSI) using a pulse width modulation (PWM) or Space Vector Modulation (SVM) algorithm. It should be pointed out that, in EV applications, the speed loop is not controlled by the prime mover and, therefore, the speed related variables (inertia and friction) and magnitude (torque disturbance) have no influence in the high speed behaviour.

### 3.2. FOC control PI adjustment in z domain

From (1) and (2) it is concluded that the plant dynamics can be simplified to a first-order system formed by a resistance and an inductance, while the back electromotive force (EMF) acts as a disturbance. Traditionally, FOC current controllers for PMSM are addressed tuning proportional and integral (PI) controllers (Fig. 2).

Although PI tuning in the Laplace domain (s domain) is sufficient in

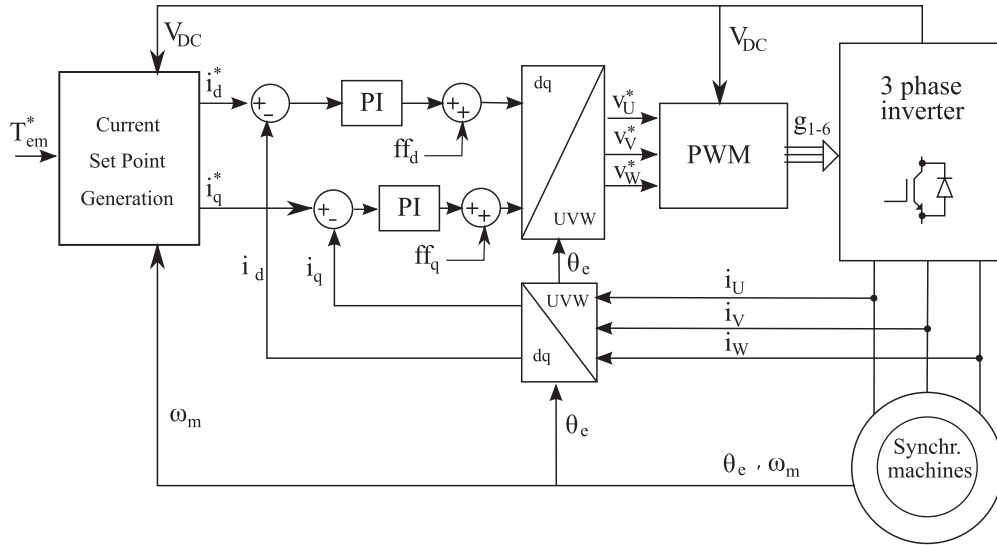


Fig. 1. Conventional FOC structure, including optimal current set point generation algorithm, PI based current regulators and Park transform.

many applications, it is advisable to tune such current PI controllers in the z domain and to include a pre-filter (PF) if high accuracy is required. Hence, the well-known zero-order hold (ZOH) transformation method [36] has been used to obtain the plant transfer function in z domain according to expression (6). Once in the z domain, the delays, which are mainly caused by the time needed by the digital signal processor (DSP) to sample the currents and execute the controllers as well as the PWM unit to synthesize the required voltage, can be easily considered in the model including a delay of one sampling period ( $z^{-1}$ ) along with the mentioned ZOH transformation method. Actually, the PWM updating mode has, with the mentioned delays, a great impact at high speed operation. Therefore, it is important to include them in the model. In this work, specifically, the voltages are initially synthesized (with the PWM) at the beginning of the following iteration after the current samples, therefore with a delay of one sample ( $z^{-1}$ ), and are finally synthesized at the end of the next iteration, i.e. with a delay of two samples ( $z^{-2}$ ). Fig. 3 shows the general block diagram to properly tune the PI controller in z domain [37], where the back EMF has been omitted for simplicity.

$$G(z) = z^{-1}(1 - z^{-1})Z\left\{\frac{G(s)}{s}\right\} = z^{-1}(1 - z^{-1})Z\left\{\frac{1/R}{s[(L/R)s + 1]}\right\} = \frac{1}{R} \frac{1 - e^{-aT}}{z(z - e^{-aT})}, \quad (6)$$

where  $a = R/L$  and  $T$  is the sampling period.

The PI controller transfer function in expression (7) is derived from PI expression in s domain when the backward Euler approximation is used [36].

$$PI(z) = K_p + K_i T \frac{z}{z - 1} = \frac{(K_p + K_i T)z - K_p}{z - 1}. \quad (7)$$

Hence, the current open-loop  $L(z)$  and closed-loop  $T(z)$  transfer functions can be deduced as indicated in expressions (8) and (9), respectively.

$$L(z) = \frac{(K_p + K_i T)z - K_p}{z - 1} \frac{1}{R} \frac{1 - e^{-aT}}{z(z - e^{-aT})}, \quad (8)$$

$$T(z) = \frac{(K_p + K_i T)(1 - e^{-aT})(z - \frac{K_p}{K_p + K_i T})}{R(z^3 + z^2(-1 - e^{-aT}) + z(e^{-aT} + \frac{1}{R}(K_p + K_i T)(1 - e^{-aT})) - \frac{K_p}{R}(1 - e^{-aT}))}.$$

If the current closed-loop transfer function had just two poles, the desired closed-loop characteristic equation would correspond to expression (10) and the specifications would be (i) settling time at 2% ( $T_{s,2\%}$ ) and (ii) damping factor ( $\xi$ ), which in this application is fixed to  $\xi = 1$  in order to avoid any overshoot.

$$z^2 - 2e^{-\omega_n T} z + e^{-2\omega_n T}, \text{ being } T_{s,2\%} = \frac{5.8}{\xi \omega_n}. \quad (10)$$

However, due to the inclusion of one sample time delay and the zero introduced by the PI, actually the closed-loop system is composed by the targeted two poles from (10) plus a third pole and a zero, labelled as  $c$  and  $b$ , respectively in (11). Notice how expression (11) matches with expression (9) of the actual current closed-loop.

$$K \frac{z - b}{(z^2 - 2e^{-\omega_n T} z + e^{-2\omega_n T})(z - c)}. \quad (11)$$

Therefore, the tuning of the PI consists in forcing expression (9) and (11) to be the same. The additional pole and zero will be cancelled by a PF, whose expression is indicated in (12) and by doing so, the current closed-loop dynamics has to perfectly match the second order system given in (10) with its specifications.

$$PF(z) = \frac{(1 - b)(z - c)}{(1 - c)(z - b)}. \quad (12)$$

Once the pole placement technique is numerically solved, expressions (13)–(16) are obtained.

$$c = 1 + e^{-aT} - 2e^{\omega_n T}, \quad (13)$$

$$K_p = \frac{Rce^{-2\omega_n T}}{1 - e^{-aT}}, \quad (14)$$

$$K_i T = \frac{R(e^{-2\omega_n T} + 2e^{-\omega_n T}c - e^{-aT})}{1 - e^{-aT}} - K_p, \quad (15)$$

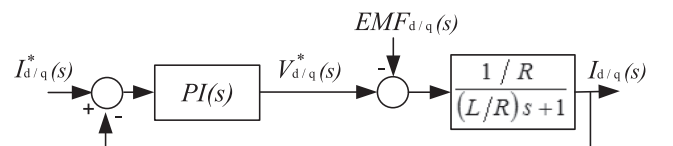


Fig. 2. Control scheme with the PI(s) controller, plant transfer function and the current, voltage and back EMF signals for the direct and quadrature axes.

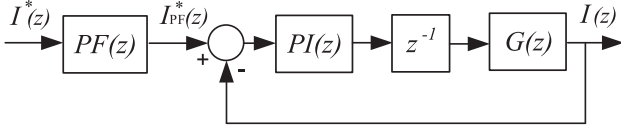


Fig. 3. Scheme for the direct and quadrature current control loop with the PI and PF controllers in  $z$  domain.

$$b = \frac{K_p}{K_p + K_i T}. \quad (16)$$

In order to illustrate the operation of a PMSM applied to EVs and HEVs, a detailed model of the propulsion system has been carried out in the Matlab/Simulink simulation environment, including PMSM, power electronics, battery and digital controllers. The three-phase inverter has been implemented as a voltage source converter using the Hydro Quebec's SimPowerSystems toolbox, while the SM-PMSM is a customized model described in the  $dq$  reference frame, including vector transformations (Clarke and Park), and expressions (1)–(3). The SM-PMSM is fed by the PWM voltages generated by the converter and the subsequent currents are feedback to the SimPowerSystems model through three variable current sources. For simplicity, the battery pack has been considered as an ideal voltage source. Finally, the control algorithms have been programmed using the model based design (MBD) approach, resulting on a real representation of an automotive electronic control unit (ECU) program.

Table 1 shows the most significant parameters of the electrical machine. As the main goal of the simulations is to study the limits of the controller at high speeds, the PMSM model does not consider any particular EV machine nor a maximum mechanical speed constraint. The values of the stator inductances, resistances, PM flux linkage and pole-pair number, are typical values found in current automotive axial flux SM-PMSMs.

Fig. 4 shows the machine current, torque and voltage regulation (under the field weakening control) for machine nominal torque and mechanical speed up to 3600 r/min, i.e. 300 Hz of electrical frequency. The traditional FOC structure of Fig. 1 is used with the PI regulators tuned as previously explained, with a damping factor of 1 and a settling time of 5 ms. Despite the fact that torque control behaves as expected, the mechanical speed is already high after 2 s and therefore the field weakening algorithm is forced to reduce the  $i_d^*$  as shown in the top trace of Fig. 4. Actually, such field weakening is required since the voltage demand is superior than the available in the DC bus.

It could be concluded that many industrial drives for standard applications perform extremely well with the FOC structure and the PI described in the previous section. Additionally, a damping factor equal to 0.707 is widely used to enlarge a bit the bandwidth; settling times between 2 ms and 10 ms are standard values and a switching frequency of 10 kHz (or a sampling time of 100  $\mu$ s) are common figures. Such a remarkable performance is obtained as long as the mechanical speeds are below (about) 6000 r/min for 3 pole-pair machines, or 3600 r/min for 5 pole-pair machines, i.e. 300 Hz. However, as it will be analyzed in the following section, with higher mechanical speeds, when the electrical frequencies increase, there will be a performance degradation and an eventual instability.

### 3.3. High speed stability problems

When conventional FOC is employed and the PMSM mechanical speed exceeds a given threshold, the torque control loop can become unstable. Fig. 5 illustrates this phenomenon which takes place before 4800 r/min or 400 Hz for the PMSM under study, regardless the commanded torque reference. In particular, torque references of 100 N·m, 50 N·m, 10 N·m and  $-50$  N·m were applied in the simulations shown in Fig. 5.

The reason for this loss of stability cannot be explained from the

control diagram depicted in Fig. 3. Such scheme does not consider vector transformations, which is adequate when the electrical frequencies are low and medium, but not when they become high. The Park transformation [38] (sometimes known as  $\alpha\beta$  to  $dq$  transformation) must be included in the model, as it has a paramount influence at high speed operation, as it is justified below. Fig. 6 shows the new complete model where, for the sake of simplicity, the PF has been removed.

In the discrete-time domain, the Park transform is defined as:

$$\begin{bmatrix} V_\alpha(nT) \\ V_\beta(nT) \end{bmatrix} = \begin{bmatrix} \cos(\omega nT) & -\sin(\omega nT) \\ \sin(\omega nT) & \cos(\omega nT) \end{bmatrix} \begin{bmatrix} V_d(nT) \\ V_q(nT) \end{bmatrix}. \quad (17)$$

The trigonometric  $z$  transform expressions given in (18) and (19) must be considered to be able to analytically express the scheme of Fig. 6 [39].

$$Z\{f(nT)\cos(\omega nT)\} = \frac{1}{2}[F(ze^{-j\omega nT}) + F(ze^{j\omega nT})], \quad (18)$$

$$Z\{f(nT)\sin(\omega nT)\} = \frac{j}{2}[F(ze^{j\omega nT}) - F(ze^{-j\omega nT})]. \quad (19)$$

Now,  $z$  domain expressions of  $\alpha\beta$  voltages correspond to (20) and (21).

$$V_\alpha(z) = \frac{1}{2}V_d(ze^{j\omega T} + ze^{-j\omega T}) - \frac{j}{2}V_q(ze^{j\omega T} + ze^{-j\omega T}), \quad (20)$$

$$V_\beta(z) = \frac{1}{2}V_q(ze^{j\omega T} + ze^{-j\omega T}) + \frac{j}{2}V_d(ze^{j\omega T} + ze^{-j\omega T}). \quad (21)$$

Following the scheme depicted in Fig. 6, the  $z$  domain expressions of  $\alpha\beta$  currents are:

$$I_\alpha(z) = G(z)V_\alpha(z) = \frac{1}{2}G(z)[V_d(ze^{j\omega T} + ze^{-j\omega T}) - jV_q(ze^{j\omega T} + ze^{-j\omega T})], \quad (22)$$

$$I_\beta(z) = G(z)V_\beta(z) = \frac{1}{2}G(z)[V_q(ze^{j\omega T} + ze^{-j\omega T}) + jV_d(ze^{j\omega T} + ze^{-j\omega T})]. \quad (23)$$

Using expressions (18) and (19),  $d$ -axis current can be obtained as follows:

$$I_d(z) = \frac{1}{2}I_\alpha(ze^{j\omega T} + ze^{-j\omega T}) + \frac{1}{2}I_\beta(ze^{j\omega T} - ze^{-j\omega T}). \quad (24)$$

Considering (22) and (23) in (24), the following equation is obtained:

$$\begin{aligned} I_d(z) = & \frac{1}{4}\{G(ze^{j\omega T})[V_d(ze^{2j\omega T} + z) - jV_q(ze^{2j\omega T} - z)] \\ & + G(ze^{-j\omega T})[V_d(z + ze^{-2j\omega T}) - jV_q(z - ze^{-2j\omega T})] \\ & + G(ze^{j\omega T})j[jV_d(ze^{2j\omega T} - z) + V_q(ze^{2j\omega T} + z)] \\ & - G(ze^{-j\omega T})j[jV_d(z - ze^{-2j\omega T}) + V_q(z + ze^{-2j\omega T})]\}. \end{aligned} \quad (25)$$

Rearranging Eq. (25), a final expression for  $I_d(z)$  (26) is deduced.

Table 1

Nominal parameters of the PMSM under study and power system.

Parameter	Value	Unit
d-axis phase inductance ( $L_d$ )	0.35	mH
q-axis phase inductance ( $L_q$ )	0.35	mH
Phase resistance ( $R_s$ )	100	m $\Omega$
PM flux linkage ( $\Psi_{PM}$ )	0.07	Wb
Pole-pair ( $P$ )	5	–
Switching frequency ( $f_{sw}$ )	10	kHz
Battery voltage ( $V_{DC}$ )	500	V
Nominal torque ( $T_{em}^{nom}$ )	100	N·m

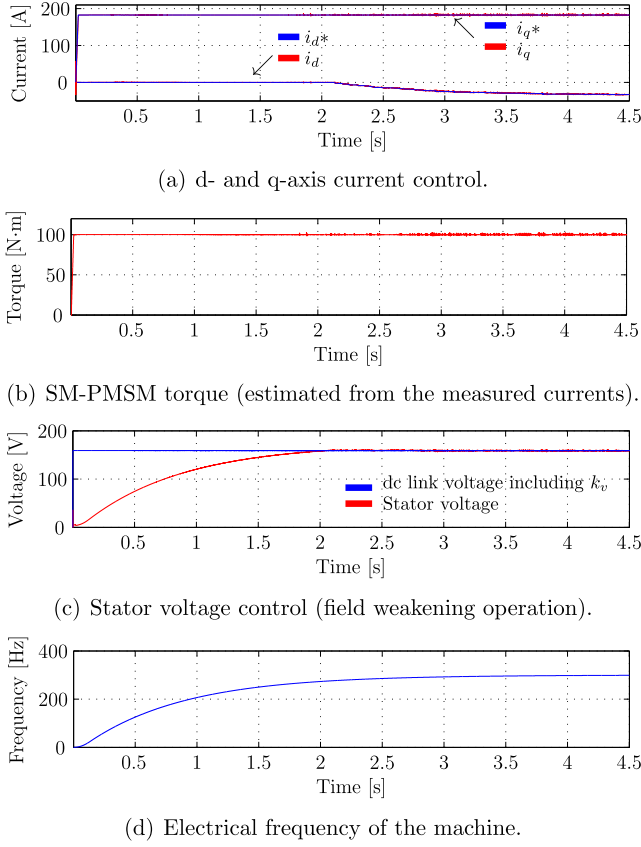


Fig. 4. Torque control results of the studied machine with conventional FOC structure up to 3600 r/min (300 Hz electrical).

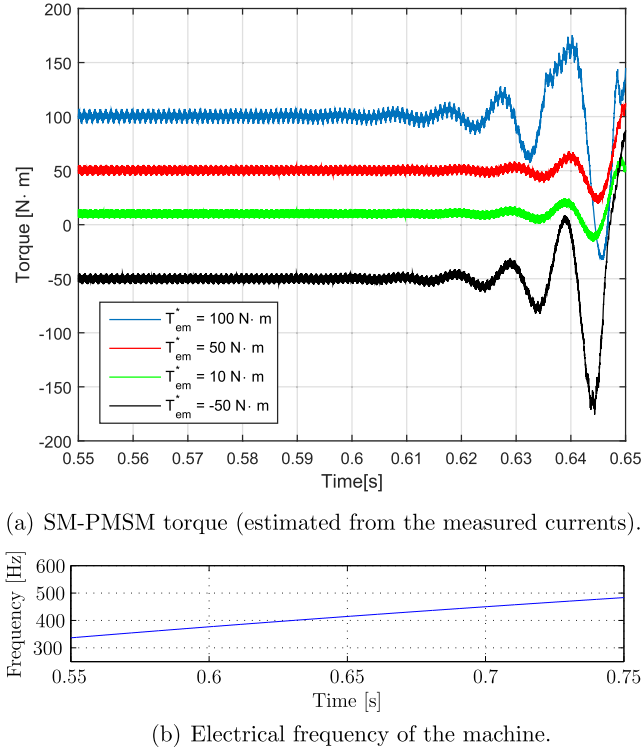


Fig. 5. Torque control instability of the studied machine with conventional FOC structure under a variety of torque regulation conditions.

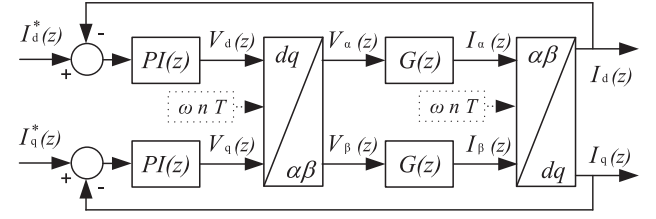


Fig. 6. Full scheme for both current control loops with the Park transformations (the PF has been removed for the sake of simplicity).

$$I_d(z) = \frac{1}{2} V_d(z) [G(z e^{j\omega T}) + G(z e^{-j\omega T})] + \frac{1}{2} V_q(z) j [G(z e^{j\omega T}) - G(z e^{-j\omega T})]. \quad (26)$$

Similarly, final expression of the q current is directly given in (27).

$$I_q(z) = -\frac{1}{2} V_d(z) j [G(z e^{j\omega T}) - G(z e^{-j\omega T})] + \frac{1}{2} V_q(z) [G(z e^{j\omega T}) + G(z e^{-j\omega T})]. \quad (27)$$

In order to obtain a compact multi input and multi output (MIMO) transfer function, direct and coupling transfer functions labelled as  $G_{AC}(z)$  and  $G_C(z)$ , respectively, are:

$$\begin{aligned} G_{AC}(z) &= \frac{1}{2} [G(z e^{j\omega T}) + G(z e^{-j\omega T})] = \frac{1 - e^{-aT}}{2R} \left( \frac{1}{z e^{j\omega T} (z e^{j\omega T} - e^{-aT})} \right) \\ &\quad + \frac{1 - e^{-aT}}{2R} \left( \frac{1}{z e^{-j\omega T} (z e^{-j\omega T} - e^{-aT})} \right) \\ &= \frac{1 - e^{-aT}}{R} \frac{z \cos(2\omega T) - e^{-aT} \cos(\omega T)}{z(z^2 - z e^{-aT} 2 \cos(\omega T) + e^{-2aT})}, \end{aligned} \quad (28)$$

$$\begin{aligned} G_C(z) &= \frac{1}{2} [G(z e^{j\omega T}) - G(z e^{-j\omega T})] \\ &= \frac{1 - e^{-aT}}{R} \frac{-z j \sin(2\omega T) + e^{-aT} j \sin(\omega T)}{z(z^2 - z e^{-aT} 2 \cos(\omega T) + e^{-2aT})}. \end{aligned} \quad (29)$$

The final MIMO transfer function is given in expression (30) and illustrated in Fig. 7(a),

$$\begin{bmatrix} I_d(z) \\ I_q(z) \end{bmatrix} = \begin{bmatrix} G_{AC}(z) & G_C(z) \\ -G_C(z) & G_{AC}(z) \end{bmatrix} \begin{bmatrix} V_d(z) \\ V_q(z) \end{bmatrix}, \quad (30)$$

from where the following partial conclusions can be drawn:

- The system is MIMO and coupled. Therefore, much more complex to control. Consequently, SISO standard tools for both control and stability cannot be used.
- Notice that, at zero frequency,  $G_C(z)$  tends to disappear and  $G_{AC}(z)$  is the same as  $G(z)$ , confirming the idea that at low electrical speeds, the PI controller is enough.

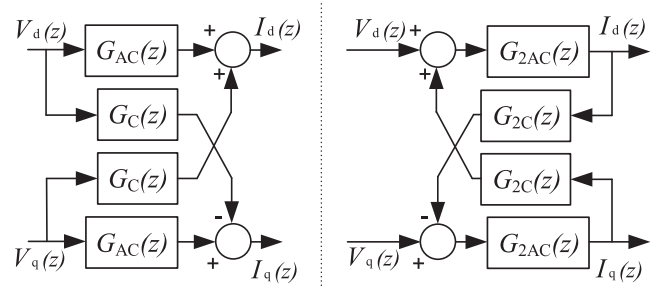


Fig. 7. PMSM model. (a) MIMO scheme given on Eq. (30). (b) Equivalent MIMO scheme.



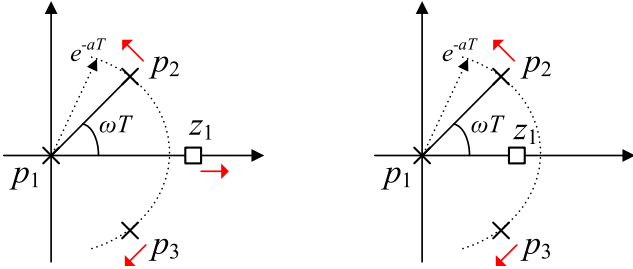


Fig. 8. (a)  $G_{AC}(z)$  and (b)  $G_C(z)$  pole-zero maps.

- The PI approach has limitations, which arise at high frequencies, the closed-loop system becomes unstable.
- $G_{AC}(z)$  and  $G_C(z)$  pole-zero maps are given in Fig. 8 a) and b), respectively. Two of the three poles have always a constant magnitude but its angle depends on the mechanical speed. The  $G_{AC}(z)$  zero moves from  $e^{-aT}$  up to  $+\infty$ , leaving rather quickly the unitary circle. Zero values, considering the PMSM data given in Table 1 and for  $T = 100 \mu s$ , are indicated in Table 2 for several electrical frequencies.

### 3.4. Numerical stability study

Given the fact that the plant under study is not linear time invariant (LTI) but linear time variant (LTV) or linear parameter variant (LPV), since the closed-loop poles are frequency dependent, as stated in (28) and (29) transfer functions collected in the final MIMO matrix transfer function (30), any attempt to obtain an analytic expression for the stability margin becomes very difficult. Nevertheless, a full numerical linear study which brings specific information about the stability limits of the plant under study is presented. The PI controller expressed in the MIMO notation is as follows:

$$\begin{bmatrix} V_d \\ V_q \end{bmatrix} = \begin{bmatrix} PI(z) & 0 \\ 0 & PI(z) \end{bmatrix} \begin{bmatrix} e_{Id} \\ e_{Iq} \end{bmatrix}, \quad (31)$$

Therefore, connecting in series (31) and (30) as deduced from Fig. 6 scheme, the open-loop expression becomes:

$$\begin{bmatrix} I_d \\ I_q \end{bmatrix} = \begin{bmatrix} G_{AC}(z)PI(z) & G_C(z)PI(z) \\ -G_C(z)PI(z) & G_{AC}(z)PI(z) \end{bmatrix} \begin{bmatrix} e_{Id} \\ e_{Iq} \end{bmatrix}. \quad (32)$$

Imposing the unitary feedback in (33) into (32) and isolating the actual currents, the final closed-loop MIMO transfer function (34) is obtained.

$$\begin{bmatrix} e_{Id} \\ e_{Iq} \end{bmatrix} = \begin{bmatrix} I_d^* \\ I_q^* \end{bmatrix} - \begin{bmatrix} 1 & 0 \\ 0 & 1 \end{bmatrix} \begin{bmatrix} I_d \\ I_q \end{bmatrix} = \begin{bmatrix} I_d^* - I_d \\ I_q^* - I_q \end{bmatrix}, \quad (33)$$

$$\begin{bmatrix} I_d \\ I_q \end{bmatrix} = \begin{bmatrix} 1 + G_{AC}(z)PI(z) & G_C(z)PI(z) \\ -G_C(z)PI(z) & 1 + G_{AC}(z)PI(z) \end{bmatrix}^{-1} \begin{bmatrix} G_{AC}(z)PI(z) & G_C(z)PI(z) \\ -G_C(z)PI(z) & G_{AC}(z)PI(z) \end{bmatrix} \begin{bmatrix} I_d^* \\ I_q^* \end{bmatrix}. \quad (34)$$

From this point onwards, the numerical values given on Table 1 of

Table 2  
 $G_{AC}(z)$  and  $G_C(z)$  zero values for several electrical frequencies.

Fe (Hz)	0	500	833	1250
$e^{-aT} \sin(\omega T) / \sin(2\omega T)$	0.49	0.51	0.56	0.69
$e^{-aT} \cos(\omega T) / \cos(2\omega T)$	0.97	1.14	1.68	$\infty$

the manuscript have been introduced and, with the help of Matlab, a minimal realization of the closed-loop matrix transfer function and its closed-loop poles are computed. The numerical results, which are printed every 25 Hz from 100 Hz until 600 Hz, are illustrated in Fig. 9, from which it can be concluded that stability is maintained for electrical frequencies lower than 521.7 Hz.

Nevertheless, in Fig. 5, the instability already appeared before 400 Hz. The explanation for this lower range of stability must be found in the inclusion of the feed-forward terms ( $ff$ ), which is quite a common practice in general purpose drives [38]. The need of the  $ff_d$  (35) and  $ff_q$  (36) terms

$$ff_d = \omega L_q i_q, \quad (35)$$

$$ff_q = -\omega(L_d i_d + \Psi_m), \quad (36)$$

arises from the analysis of the dq PMSMs representation given in (1) and (2) and their inclusion is illustrated in Fig. 1.

Instead of applying the unitary feedback as previously done in the open-loop MIMO transfer function (32), now the following feedback expression must be considered<sup>1</sup>:

$$\begin{bmatrix} e_{Id} \\ e_{Iq} \end{bmatrix} = \begin{bmatrix} I_d^* \\ I_q^* \end{bmatrix} - \begin{bmatrix} 1 & \frac{\omega L_q}{PI(z)} \\ -\frac{\omega L_d}{PI(z)} & 1 \end{bmatrix} \begin{bmatrix} I_d \\ I_q \end{bmatrix}. \quad (37)$$

The numerical analysis has been repeated from 100 Hz to 450 Hz and the results obtained, which are illustrated in Fig. 10, confirm the reduction of the stability down to 379.8 Hz.

From this numerical study, the following partial conclusions can be derived:

- The frequency stability limit can be numerically computed in advance (for any experimental implementation).
- An excellent match of the computed maximum operating frequencies exists between the time results and the MIMO closed-loop poles, which confirms the validity of the approach presented in this subsection and Section 3.3.
- The extended use of feed-forward terms (35) and (36), despite improving the FOC performance at standard speeds, drastically reduces the stability margin when the speed increases. In this specific scenario, the stability limit is reduced from 521.7 Hz down to 379.8 Hz, which strongly agrees with the result illustrated in Fig. 5.

### 3.5. Discussion about the limits of the decoupling

Decoupling is a common way to reduce any MIMO and coupled system into a SISO. The decoupling may be achieved pre multiplying expression (30) as indicated in (38), where the decoupling transfer function  $D(z)$  is given in (39). However, the unique pole of such decoupling controller  $D(z)$  will already be outside the unitary circle even for low values of electrical frequency and therefore will be unstable, as it can be deduced from the data given in Table 2.

$$\begin{bmatrix} I_d(z) \\ I_q(z) \end{bmatrix} = \begin{bmatrix} G_{AC}(z) & G_C(z) \\ -G_C(z) & G_{AC}(z) \end{bmatrix} \begin{bmatrix} 1(z) & -D(z) \\ D(z) & 1 \end{bmatrix} \begin{bmatrix} V_d(z) \\ V_q(z) \end{bmatrix} \\ = \begin{bmatrix} G_{AC}(z) + G_C(z)^2/G_{AC}(z) & -G_{AC}(z)G_C(z)/G_{AC}(z) \\ G_{AC}(z)G_C(z)/G_{AC} - G_C(z) & G_{AC}(z) + G_C(z)^2/G_{AC}(z) \end{bmatrix} \begin{bmatrix} V_d(z) \\ V_q(z) \end{bmatrix}. \quad (38)$$

<sup>1</sup> The  $PI(z)$  appears dividing the  $ff$  terms because they have been moved (to the left hand side of Fig. 1 scheme) up to the error comparator.

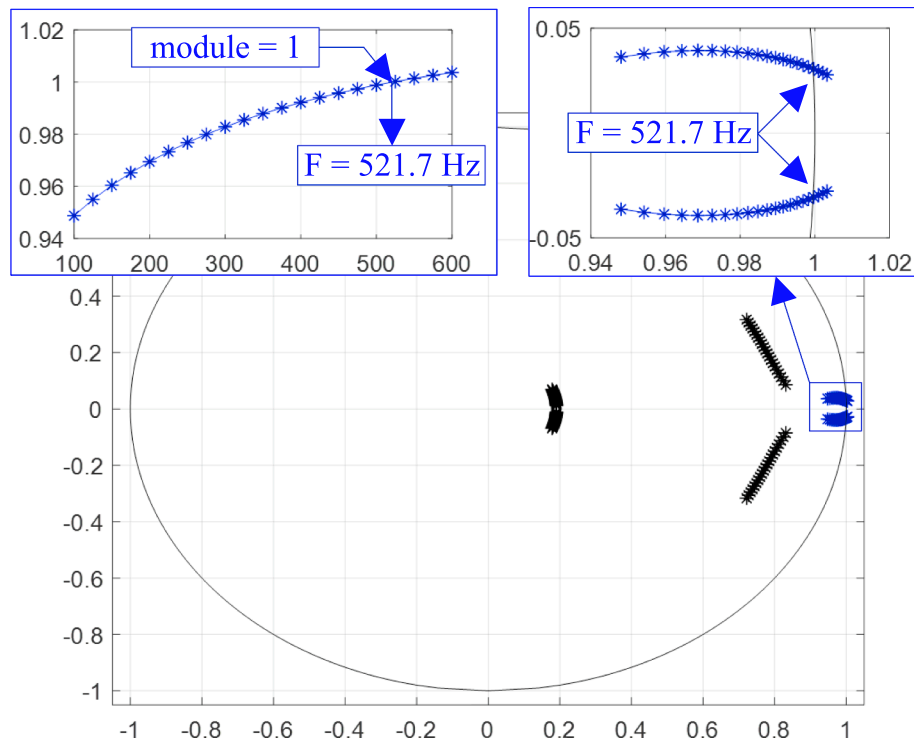


**Fig. 9.** Evolution (from 100 Hz up to 600 Hz) of the six closed-loop poles of the whole MIMO system (34). The two closed-loop poles, which crosses the unitary circle for a frequency equal to 521.7 Hz, are zoomed in and its module growth is also detailed.

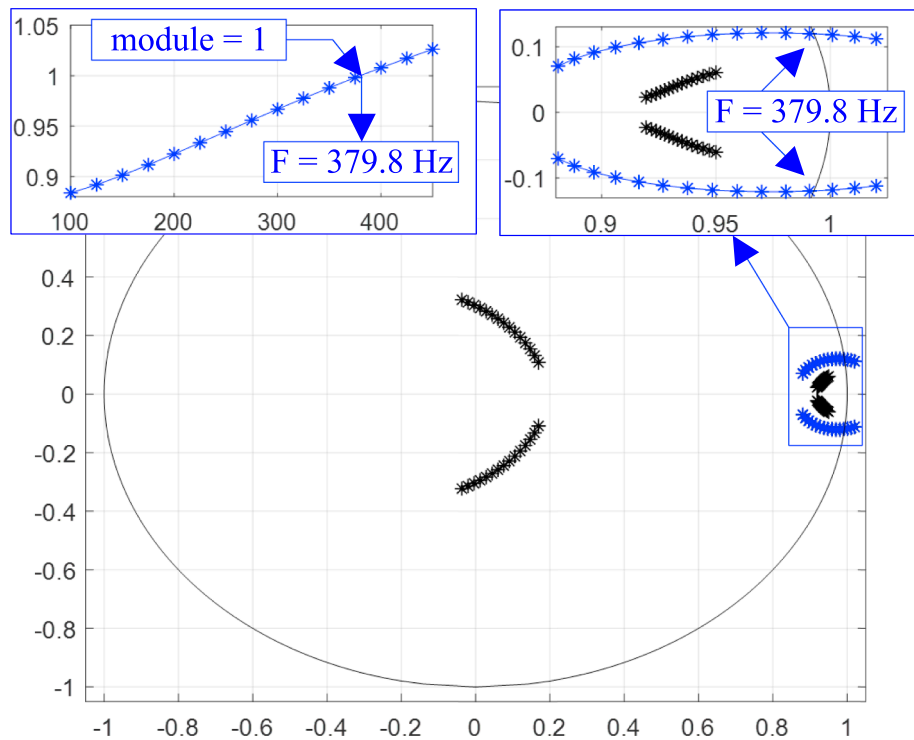


**Fig. 10.** Evolution (from 100 Hz up to 450 Hz) of the six closed-loop poles of the whole MIMO system which includes the feed-forward terms. The two closed-loop poles, which crosses the unitary circle for a frequency equal to 379.8 Hz, are zoomed in and its module growth is also detailed.

$$D(z) = \frac{G_C(z)}{G_{AC}(z)} = \frac{z \sin(2wT) - e^{-aT} \sin(wT)}{z \cos(2wT) - e^{-aT} \cos(wT)}. \quad (39)$$

#### 4. Proposed controller

An alternative but equivalent MIMO system is generated as illustrated in Fig. 7 b) in order to avoid the lack of decoupling introduced by (30). The new transfer functions are given in (40) and (41) and the decoupling transfer function  $D_2(z)$  must be equal to (41). It is obvious that such  $D_2(z)$  transfer function is non causal and therefore could not be implemented in real time.

$$G_{2AC}(z) = \frac{1 - e^{-aT}}{R} \frac{1}{z(z \cos(2wT) + e^{-aT} \cos(wT))}, \quad (40)$$

$$G_{2C}(z) = \frac{R}{1 - e^{-aT}} \frac{z(z \sin(2wT) + e^{-aT} \sin(wT))}{1}, \quad (41)$$

##### 4.1. Decoupling: from MIMO to SISO

The whole decoupling algorithm is presented inside the red dashed line of Fig. 11. The proposed solution consists on estimating the current plant currents  $\hat{i}(k+1)$  and  $\hat{i}(k+2)$  for both d and q axes. Such estimation is carried out supplying to the closed-loop transfer function  $T_2(z)$  the current reference values, and delaying such reference values two iterations to the actual controller. Assuming perfect decoupling, the equivalent closed-loop transfer function would be as indicated in (42). Such delay won't compromise at all the overall performance since it is much smaller than the current closed-loop dynamics.

$$T_2(z) = \frac{C_2(z)G_{2AC}(z)}{1 + C_2(z)G_{2AC}(z)} = \frac{\text{num}_{C_2(z)}\text{num}_{G_{2AC}(z)}}{\text{den}_{C_2(z)}\text{den}_{G_{2AC}(z)} + \text{num}_{C_2(z)}\text{num}_{G_{2AC}(z)}}. \quad (42)$$

##### 4.2. Speed-adaptive controller design

Once the equivalent MIMO system is decoupled, the system is effectively reduced to a SISO system, formed by the plant  $G_{2AC}(z)$  and the controller  $C_2(z)$ . The handicap is that the new plant has got two poles, one at the origin, but the second one moving according to speed (Fig. 12) as indicated in Eq. (40). Some numerical values of this moving pole are indicated on the third row of Table 2, from where it can be seen that it moves rapidly outside the unitary circle and therefore the stable region and takes the value infinity for an electrical frequency equal to 1/8 of the sampling frequency. Therefore, no compensator will exist to stabilize the plant at that speed value, which constitutes the main limitation of this proposed controller. Another approach, which enlarges further than 1/8 of the sampling frequency, is proposed in [40,41]; however, this approach is not accurate enough to allow analytical tuning methods, such as pole placement. It is obvious then, that if the controller  $C_2(z)$  is meant to keep the closed-loop poles at the same position,  $C_2(z)$  must be adaptive. Pole placement is the methodology used to design such controller. The specifications are (i) to include an integrator to cancel the 0 type error, (ii) guarantee the settling time at 2% ( $T_{s,2\%}$ ) and (iii) avoid any overshoot  $\xi = 1$ , as it was already mentioned in Eq. (10). According to general control theory [36], the number of coefficients required by the controller in order to place the closed-loop where dictated by the specifications, must be equal to the number of the closed-loop poles. The three coefficients  $n_2$ ,  $n_1$  and  $n_0$  should be enough; however, the controller would be non causal. Therefore, a second pole is added to the controller  $C_2(z)$  as indicated in (43).

$$C_2(z) = \frac{n_0 z^2 + n_1 z + n_2}{(z-1)(d_1 z + d_2)}, \quad (43)$$

The two dominant closed-loop poles will be forced to have a settling

time at two percent of 5 ms and the remaining two will be five times faster, i.e. 1 ms; as indicated in the first part of Eq. (44). All four closed-loop poles will have a damping factor equal to 1. The right hand side of Eq. (44) corresponds to the  $\text{den}_{T_2(z)}$  already defined in Eq. (42).

$$\begin{aligned} (z^2 - 2ze^{-\frac{5.8T}{0.005}} + e^{-2\frac{5.8T}{0.005}})(z^2 - 2ze^{-\frac{5.8T}{0.001}} + e^{-2\frac{5.8T}{0.001}}) &= \text{den}_{T_2(z)} \\ &= (1 - e^{-aT})(n_0 z^2 + n_1 z + n_2) \\ &\quad + Rz[(z \cos(2wT) + e^{-aT} \cos(wT))(z \\ &\quad - 1)(d_1 z + d_2)] \end{aligned} \quad (44)$$

Solving Eq. (44), the coefficients expressions are obtained as follows:

$$d_1 = \frac{1}{\cos(2wT)}, \quad (45)$$

$$d_2 = d_1^2[-1.9007 \cos(2wT) + 0.9718 \cos(wT)], \quad (46)$$

$$n_0 = d_1^2[4.2602 \cos(2wT)^2 - 6.5580 \cos(2wT) + 3.3530 \cos(wT)^2], \quad (47)$$

$$n_1 = d_1^2[-5.1345 \cos(2wT)^2 + 6.5580 \cos(2wT) - 3.3530 \cos(wT)^2], \quad (48)$$

$$n_2 = 0.8825. \quad (49)$$

It is clear that four coefficients need to be calculated on line since they depend on the electrical angular speed. Nevertheless, considering that the speed, specially in EV and HEV, has a much slower dynamics than the current, there is no need to update such coefficients at the current rate, i.e. every sampling period  $T$ ; bringing the possibility to reduce the processor capability.

Finally, in order to just have the four poles in the current closed-loop specified in (44), a PF, whose transfer function is indicated in (50), needs to be introduced to cancel the two zeros from  $\text{num}_{C_2(z)}$ .

$$PF_2(z) = \frac{n_0 + n_1 z + n_2}{n_0 z^2 + n_1 z + n_2}. \quad (50)$$

##### 4.3. Numerical stability study

The new MIMO speed-adaptive controller, illustrated in Fig. 11, can be expressed as follows:

$$\begin{aligned} \begin{bmatrix} V_d \\ V_q \end{bmatrix} &= \begin{bmatrix} -C_2(z) & 0 \\ 0 & -C_2(z) \end{bmatrix} \begin{bmatrix} I_d \\ I_q \end{bmatrix} \\ &\quad + \begin{bmatrix} z^{-2}PF_2(z)C_2(z) & -T_2(z)D_2(z) \\ T_2(z)D_2(z) & z^{-2}PF_2(z)C_2(z) \end{bmatrix} \begin{bmatrix} I_d^* \\ I_q^* \end{bmatrix}. \end{aligned} \quad (51)$$

The plant defined in (30) is considered in (51) and, after proper matrix manipulation, the closed-loop transfer function matrix becomes:

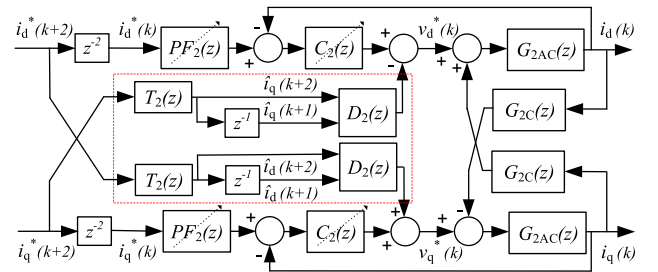
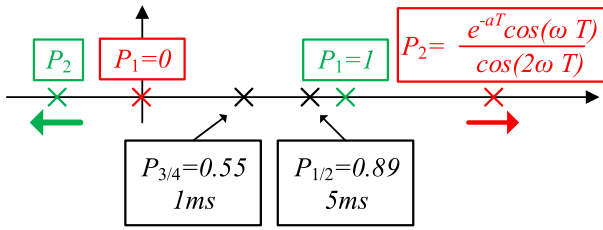


Fig. 11. Proposed adaptive control structure for PMSM high speed operation. Inside the red dashed line the decoupling controller. (For interpretation of the references to color in this figure legend, the reader is referred to the web version of this article.)





**Fig. 12.** Pole map of  $C_2(z)$  in green,  $G_{AC2}(z)$  in red and the targeted closed-loop in black. Notice how the  $P_2$  of the  $G_{AC2}(z)$  and the  $P_2$  of the  $C_2(z)$  move depending on the speed. (For interpretation of the references to color in this figure legend, the reader is referred to the web version of this article.)

$$\begin{bmatrix} I_d \\ I_q \end{bmatrix} = \left[ \begin{bmatrix} G_{AC}(z) & G_C(z) \\ -G_C(z) & G_{AC}(z) \end{bmatrix}^{-1} + \begin{bmatrix} C_2(z) & 0 \\ 0 & C_2(z) \end{bmatrix} \right]^{-1} \cdot \begin{bmatrix} z^{-2}PF_2(z)C_2(z) & -T_2(z)D_2(z) \\ T_2(z)D_2(z) & z^{-2}PF_2(z)C_2(z) \end{bmatrix} \begin{bmatrix} I_d^* \\ I_q^* \end{bmatrix} \quad (52)$$

The numerical analysis of the closed-loop poles (from 950 Hz up to 1050 Hz, with increments of 10 Hz) is illustrated in Fig. 13. From the 20 poles of the closed-loop MIMO system, just two poles cross the stability region at 1021 Hz.

The numerical analysis confirms the superior performance of the proposed speed-adaptive controller over the standard PIs, increasing the stability limit up to 1021 Hz for this specific PMSM.

#### 4.4. Results and final discussion

The numerical results of Fig. 14 show the effectiveness of the proposed controller, where the system remains stable up to 1000 Hz. Small current ripple in the d and q current waveforms can be spotted, which

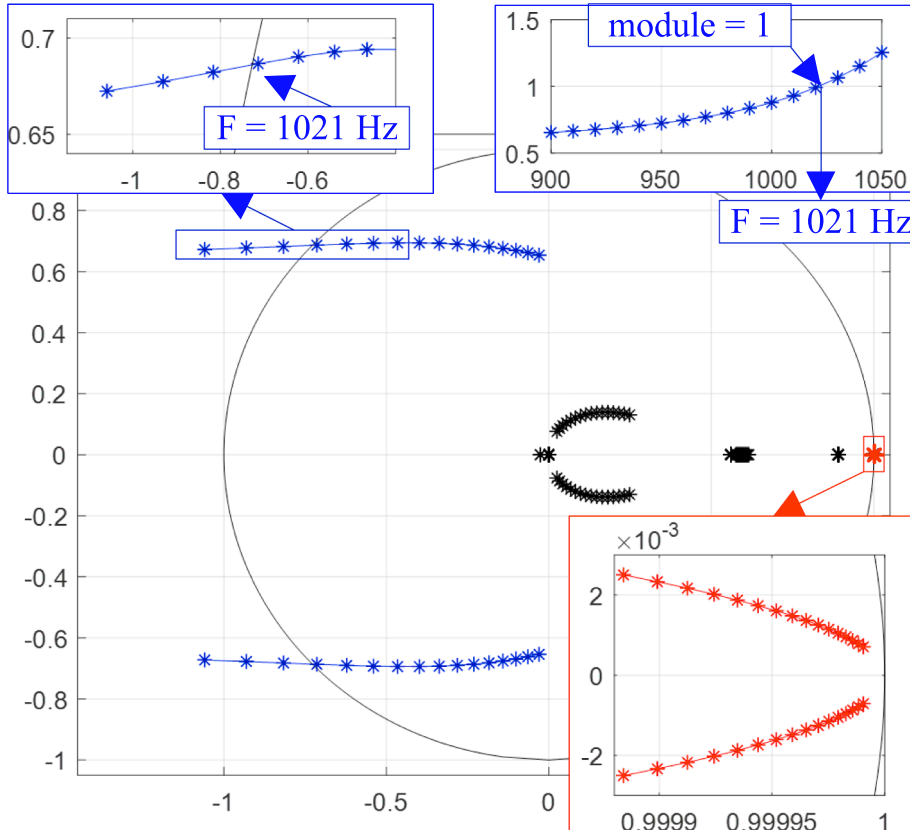


**Fig. 13.** Evolution (from 900 Hz up to 1050 Hz) of the twenty closed-loop poles of the whole MIMO proposed system (52) which includes the adaptive controller and the decoupling network. The two closed-loop poles, which crosses the unitary circle for a frequency equal to 1021 Hz, are zoomed in and its module growth is also detailed..

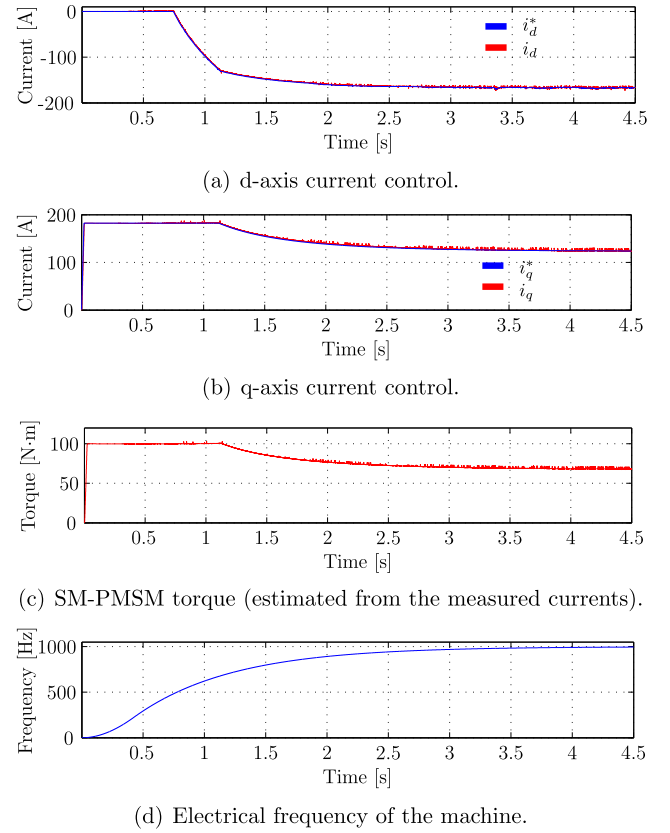


**Fig. 14.** Torque control results of the studied machine with proposed control up to 1000 Hz (electrical).

**Table 3**

Relevant Pole Zero values of the equivalent MIMO for several electrical frequencies.

Fe (Hz)	0	250	500	833	1000	1036	1100
$\frac{e^{-aT} \cos(\omega T)}{\cos(2\omega T)}$	0.97	1.01	1.14	1.68	2.54	2.91	3.99
pole $P_2 C_2(z)$	0.92	0.89	0.76	0.22	−0.64	−1.008	−2.09
zero 1 $C_2(z)$	0.91	0.92	0.97	0.99	0.99	0.99	0.99
zero 2 $C_2(z)$	0.91	0.89	0.77	0.30	0.08	0.06	0.03

are due to the existing PWM modulation and power electronics converter both included in the accurate and detailed simulation model. Such ripple is transmitted to PMSM torque; however, due to the large inertia of the EV and HEV, it will not affect the mechanical speed. It should also be noticed that a high and unrealistic acceleration has been imposed to the model to reduce simulation runtime. Actually, the smoother the speed variations, the better the controller reacts.

Also, the  $i_d^*$  is dropped up to  $-180$  A since the electrical speed is so high that the PMSM back electromagnetic force would be much larger than the available DC bus voltage. Consequently, a field weakening strategy must be introduced to keep the PMSM under control and this is the reason for such  $i_d^*$  reduction. 1000 Hz implies such a high speed that the current for the field weakening, i.e.  $i_d$ , is even larger than the torque current  $i_q$ .

The upper limit of the proposed adaptive controller depends on the (i) electrical frequency and (ii) the sampling period. For the application presented in this work, where the sampling period is  $100 \mu s$  and the PMSM parameters are listed in Table 1, it has been found that once the electrical speed reaches 1036 Hz, the controller pole from  $C_2(z)$  lies outside the unitary circle and takes the value  $-1.008$  (Table 3). This breaks the internal stability and, as corroborated in the numerical simulation, brings instability. In this case, this partial SISO analysis strongly agrees with the conclusion from sub Section 4.3 where the numerical MIMO analysis gave 1021 Hz as a maximum stable frequency.

## 5. Conclusion

The lack of controllability in traditional PI based FOC for PMSMs at high speeds has been described and analytically addressed. A comprehensive discrete-time domain formulation of the plant, which includes all the unaffordable simplifications commonly (and mistakenly) assumed by the Park transform, has been mathematically developed.

With the new discrete-time domain model, a new  $z$  domain speed-adaptive current (torque) controller for PMSM, which increases the maximum operating speed and fulfils the standard specifications, has been designed based on the pole placement technique. Moreover, an accurate numerical methodology in  $z$  domain, which computes, in advance of any experimentation, the maximum stable frequency of any given controller has been fully detailed. Such numerical methodology constitutes an extremely useful tool equivalent to stability margin techniques. The numerical results, obtained from an EV propulsion accurate model, entails that with this novel design the EV mechanical speed has been enlarged from 4800 r/min (for the traditional FOC) up to 12,000 r/min. Even more important than the speed increment achieved, it is the validation of the whole numerical stability analysis and the formulated model. Given the fact that the actual trend for the next generation of EVs and HEVs is to increase the mechanical speed, this research might have an impact not only in the scientific community but also in the applied or practical engineers.

Finally, the authors believe that the model and the numerical stability analysis presented can be used with success, not only in FOC based electrical machine drives, but also in grid connected converters.

## Acknowledgements

The present work has been supported by the Government of Spain through the *Agencia Estatal de Investigación* under the Projects DPI2017-85404-P and DPI2014-53685-C2-2-R, by the *Generalitat de Catalunya* through the Project 2017 SGR 872, as well as for the research projects ENSOL (KK-2018/00040), SICSOL (KK-2018/00064) and GANICS (KK-2017/00050), within the ELKARTEK program of the Government of the Basque Country. Also, this work has been supported by the Department of Education, Linguistic Policy and Culture of the Basque Government within the fund for research groups of the Basque university system IT978-16.

## References

- [1] Global EV outlook 2018: towards cross-modal electrification. Tech. rep. International Energy Agency; 2018.
- [2] Domínguez-Navarro J, Dufo-López R, Yusta-Loyo J, Artal-Sevil J, Bernal-Agustín J. Design of an electric vehicle fast-charging station with integration of renewable energy and storage systems. *Int J Electr Power Energy Syst* 2019;105:46–58.
- [3] Sadeghianpourhamami N, Refa N, Strobbe M, Devellder C. Quantitative analysis of electric vehicle flexibility: a data-driven approach. *Int J Electr Power Energy Syst* 2018;95:451–62.
- [4] Boldea I, Tutelea L, Parsa L, Dorrell D. Automotive electric propulsion systems with reduced or no permanent magnet: an overview. *IEEE Trans Industr Electron* 2014;61(10):5696–711.
- [5] Riba J, López-Torres C, Romeral L, Garcia. Rare-earth-free propulsion motors for electric vehicles: a technology review. *Renew Sustain Energy Rev* 2016;57:367–79.
- [6] Belhadi M, Krebs G, Marchand C, Hannoun H. Evaluation of axial SRM for electric vehicle application. *Electr Power Syst Res* 2017;148:155–61.
- [7] Carpiuc S, Lazar C. Modeling of synchronous electric machines for real-time simulation and automotive applications. *J Franklin Inst* 2017;354:6258–81.
- [8] Finken T, Hombitzer M, Hameyer K. Study and comparison of several permanent-magnet excited rotor types regarding their applicability in electric vehicles. In: *Proc. of the electrical power train conference (Emobility)*; 2010.
- [9] Chaoui H, Khyamy M, Okoye O. MTPA based operation point speed tracking for PMSM drives without explicit current regulation. *Electr Power Syst Res* 2017;151:125–35.
- [10] Boubaker N, Matt D, Enrici P, Nierlich F, Durand G, Orlandini F, et al. Study of eddy-current loss in the sleeves and Sm-Co magnets of a high-performance SMPM synchronous machine (10 kRPM, 60 kW). *Electr Power Syst Res* 2017;142:20–8.
- [11] Feng G, Lai C, Iyer K, Kar N. Improved high-frequency voltage injection based permanent magnet temperature estimation for PMSM condition monitoring for EV applications. *IEEE Trans Veh Technol* 2018;67(1):216–25.
- [12] Jung S, Hong J, Nam K. Current minimizing torque control of the IPMSM using Ferrari's method. *IEEE Trans Power Electron* 2013;28(12):5603–17.
- [13] Lara J, Xu J, Chandra A. Effects of rotor position error in the performance of field-oriented-controlled PMSM drives for electric vehicle traction applications. *IEEE Trans Industr Electron* 2016;63(8):4738–51.
- [14] Fodorean D, Sarrazin M, Martis C, Anthonis J, Van der Auweraer H. Electromagnetic and structural analysis for a surface-mounted PMSM used for light-EV. *IEEE Trans Industr Electron* 2016;52(4):2892–9.
- [15] Fodorean D, Idoumghar L, Brevilliers M, Minciunescu P, Irima C. Hybrid differential evolution algorithm employed for the optimum design of a high-speed PMSM used for EV propulsion. *IEEE Trans Industr Electron* 2017;64(12):9824–33.
- [16] Popa D, Fodorean D. Design and performances evaluation of a high speed induction motor used for the propulsion of an electric vehicle. *Proc. of the international symposium on power electronics, electrical drives, automation and control*. 2014. p. 88–93.
- [17] Shue S, Pan C. Voltage-constraint-tracking-based field-weakening control of IPM synchronous motor drives. *IEEE Trans Industr Electron* 2008;55(1):340–7.
- [18] Meyer M, Bocker J. Optimum control for interior permanent magnet synchronous motors (IPMSM) in constant torque and flux weakening range. In: *Proc. of the EPE-PEMC conference*; 2006. p. 282–6.
- [19] Fall O, Nguyen N, Charpentier J, Letellier P, Semail E, Kestelyn X. Variable speed control of a 5-phase permanent magnet synchronous generator including voltage and current limits in healthy and open-circuited modes. *Electr Power Syst Res* 2016;140:507–16.
- [20] Niu F, Wang B, Babel A, Li K. Comparative evaluation of direct torque control strategies for permanent magnet synchronous machines. *IEEE Trans Power Electron* 2015;31(2):1408–24.
- [21] Hassan A, Shehata E. High performance direct torque control schemes for an IPMSM drive. *Electr Power Syst Res* 2012;89:171–82.
- [22] Rocha-Osorio CM, Solís-Chaves J, Casella R, Capovilla C, Azcue-Puma J, Sguarez-Filho A. GPRS/EGPRS standards applied to DTC of a DFIG using fuzzy PI controllers. *Int J Electr Power Energy Syst* 2017;93:365–73.
- [23] Khooban MH, Vafamand N, Niknam T. T-S fuzzy model predictive speed control of electrical vehicles. *ISA Trans* 2016;64:231–40.
- [24] Niu H, Yu J, Yu H, Lin C, Zhao L. Adaptive fuzzy output feedback and command filtering error compensation control for permanent magnet synchronous motors in electric vehicle drive systems. *J Franklin Inst* 2017;354:6610–29.

- [25] Yu J, Shi P, Dong W, Lin C. Reduced-order observer-based adaptive fuzzy tracking control for chaotic permanent magnet synchronous motors. *Neurocomputing* 2016;214(19):201–9.
- [26] Pellegrino G, Armando E, Guglielmi P. Optimal exploitation of the constant power region of IPM drives based on field oriented control. In: *Proc. of the IEEE industry applications conference*; 2007. p. 1335–40.
- [27] Chinchilla M, Arnaltes S, Burgos J. Control of permanent-magnet generators applied to variable-speed wind energy system connected to the grid. *IEEE Trans Energy Convers* 2006;87(1):130–5.
- [28] Lara J, Chandra A. Performance investigation of two novel HSFSI demodulation algorithms for encoderless FOC of PMSMs intended for EV propulsion. *IEEE Trans Industr Electron* 2018;65(2):1074–83.
- [29] Tang Z, Akin B. A new LMS algorithm based deadtime compensation method for PMSM FOC drives. *IEEE Trans Ind Appl* 2018;54(6):6472–84.
- [30] Ben-Said-Romdhane M, Naouar M, Slama-Belkhdja I, Monmasson E. Time delay consideration for robust capacitor-current-inner-loop active damping of LCL-filter-based grid-connected converters. *Int J Electr Power Energy Syst* 2018;95:177–87.
- [31] Geddada N, Mishra M, Manoj Kumar M. SRF based current controller using PI and HC regulators for DSTATCOM with SPWM switching. *Int J Electr Power Energy Syst* 2015;67:87–100.
- [32] Taha W, Beig AR, Boiko I. Quasi optimum PI controller tuning rules for a grid-connected three phase AC to DC PWM rectifier. *Int J Electr Power Energy Syst* 2018;96:74–85.
- [33] Morimoto S, Takeda Y, Hirasu T, Taniguchi K. Expansion of operating limits for permanent magnet motor by current vector control considering inverter capacity. *IEEE Trans Ind Appl* 1990;26(5):866–71.
- [34] Morimoto S, Tong Y, Takeda Y, Hirasu T. Loss minimization control of permanent magnet synchronous motor drives. *IEEE Trans Industr Electron* 1994;41(5):511–7.
- [35] Trancho E, Ibarra E, Arias A, Kortabarria I, Jurgens J, Marengo L, et al. PM-assisted synchronous reluctance machine flux weakening control for EV and HEV applications. *IEEE Trans Industr Electron* 2018;65(4):2986–95.
- [36] Ogata K. *Discrete-time control systems*. Prentice-Hall; 1995.
- [37] Arias A, Caum J, Griñó R. Moving towards the maximum speed in stepping motors by means of enlarging the bandwidth of the current controller. *Mechatronics* 2016;40:51–62.
- [38] Mohan N. *Advanced electric drives*. Wiley; 2014.
- [39] Malo S, Griñó R. Adaptive feed-forward cancellation control of a full-bridge DC-AC voltage inverter. In: *Proc. of the international federation of automatic control world congress (IFAC)*; 2008. p. 4571–6.
- [40] Bae B, Sul S. A compensation method for time delay of full-digital synchronous frame current regulator of PWM AC drives. *IEEE Trans Ind Appl* 2003;39(3):802–10.
- [41] Yim J, Sul S, Bae B, Patel N, Hiti S. Modified current control schemes for high-performance permanent-magnet ac drives with low sampling to operating frequency ratio. *IEEE Trans Ind Appl* 2009;45(2):763–71.